Incorporation of Europium(III) into Scheelite-Related Host Matrices ABO4 (A = Ca2+, Sr2+, Ba2+; B = W6+, Mo6+): Role of A- and B- Sites on the Dopant Site-Distribution and Photoluminescence

Xiao, B.; Schmidt, M.;

Originally published:

November 2017

Inorganic Chemistry 56(2017), 14948-14959

DOI: https://doi.org/10.1021/acs.inorgchem.7b02211

Incorporation of Europium(III) into Scheelite-Related Host Matrices ABO_4 ($A = Ca^{2+}, Sr^{2+}, Ba^{2+}$; $B = W^{6+}, Mo^{6+}$): Role of A- and B- Sites on the Dopant Site-Distribution and Photoluminescence

Bin Xiao[a] *and Moritz Schmidt*[a,]*

[a]Helmholtz-Zentrum Dresden – Rossendorf, Institute of Resource Ecology, Bautzner Landstraße 400, 01328 Dresden, Germany

Abstract

Scheelite and powellite related materials doped with trivalent lanthanides or actinides have been the subject of extensive research due to their important role in mineralogical, technological and environmental implications. Detailed structural knowledge of these solid solutions is essential for understanding their physicochemical properties and predicting material properties. In this work, we conduct a comprehensive spectroscopic analysis by means of polarization-dependent site-selective time resolved laser-induced fluorescence spectroscopy (p-TRLFS), to delineate the influence of the host phase cations for a series of scheelite-type matrices based on a general formulae of ABO_4 (A = Ca^{2+}, Sr^{2+}, Ba^{2+}; B = W^{6+}, Mo^{6+}) on the local environment of the Eu^{3+} dopant. Eu^{3+} has been used as a luminescent probe to access the local structural environment of crystalline substitutional sites suitable for trivalent lanthanides or actinides occupation. Our results show that the lattice distortion is overall minor, but increases with increasing mismatch of host and guest cation size. We observe a linear dependence of Eu^{3+}'s excitation energy on the host cation size and the A – O bond distance, which can be used to determine the hitherto unknown Eu – O bond distance in $NaEu(WO_4)_2$. A value of 2.510 Å was determined, somewhat larger than a previously reported number for $NaEu(MoO_4)_2$. The results also show clear evidence that the local coordination environment of Eu in WO_4^{2-} materials is more symmetrical than in their isostructural MoO_4^{2-} counterparts. The detailed spectroscopic interpretation conducted in this study resolves the relation between local distortion around a dopant and the host phase cations in structural disordered materials and may give novel insights with respect to rational design and tailoring of functional materials.

Introduction

Calcium ortho-tungstates and -molybdates are a family of naturally occurring minerals that have been studied extensively recent decades. The minerals are named scheelite ($CaWO_4$) and powellite ($CaMoO_4$), respectively. Scheelite is the most important economic W mineral, and it can be found in a wide variety of environmental conditions, including hydrothermal veins, metamorphic strata bound deposits, and skarns.[1] Both scheelite and powellite have a large number of synthetic derivatives that are based on a general formula $A_n(BO_4)_m$, where both cation sites, A and B, can be occupied by a wide variety of elements, Na, K, Rb, Ca, Sr, Pb, Ba, Zn, Cd, In, Ga, Tl, Ln, Y, and Bi, and Mo, W, Nb, V, Ta, respectively.[2] Due to their high stability and relative ease of preparation, they have found many industrial applications as solid oxide fuel cells,[3, 4] photocatalysts,[5] and luminescent materials holding immense promise for lighting and displays.[6, 7] Typically, the functional materials are solid solutions with a lanthanide dopant in the A position.

Recently, much of the interest in preparation and study of scheelite-type materials arises from their exceptional compositional variability, which allows for the easy formation of solid solutions by accommodating a wide range of chemical substitutions As this includes trivalent lanthanides (Ln^{3+}) and actinides (An^{3+}), powellite is currently actively studied in the context of nuclear waste management.[8-10] Mo is a high-yield fission product, and powellite is one of the primary Mo-containing crystalline phases that may form in high-level nuclear waste (HLW) borosilicate glasses during waste processing.[8] In particular, powellite-rich solid solutions with noteworthy chemical durability gathered wide attention due to the importance of these phases for the immobilization of highly radiotoxic Np, Pu, and Am from nuclear wastes.[8, 11, 12]

The thermodynamic stability of these solid solutions is largely dependent on their structural deviation from the stoichiometric phases and the lattice strain associated with this deviation.[13] Likewise, the performance of scheelite-based materials for their various applications will depend on their crystal structure. In particular for luminescence applications the local coordination of the luminescent dopant will directly affect their usefulness.[2] Understanding how the host structure affects the local coordination environment of a dopant will make the difference between trial-and-error material synthesis and the *a priori* development of materials tailored for a specific purpose. On the bulk level, scheelite-type materials are isostructural and crystallize with tetragonal crystal symmetry in the space group $I4_1/a$.[14, 15] Within the structure, each divalent A^{2+} is bound to eight O atoms, forming an AO_8 square antiprism, while the hexavalent W^{6+}/Mo^{6+} sites are connected with four O atoms, resulting in a tetragonal coordination geometry. Due to the nearly identical ionic radii of W^{6+} and Mo^{6+} (42 and 41 pm, respectively[16]), the lattice parameters are nearly identical for compounds with the same A site cation. In doped materials, however, structural disorder may provide a distribution of local cationic environments around the doping sites, which will deviate from that of the crystallographic sites, attributable to size and charge mismatch of the dopant and the coexistence of mono-, di- and trivalent cations randomly located in the host lattice.[17, 18] However, X-ray or neutron diffraction can merely yield an “averaged” image of the unit cell content. The structural details behind such disordered substitution, such as specific ionic environment around dopants,[19] number of non-equivalent doping species[18, 20] as well as spatial accommodation of doping centers,[21, 22] are difficult or impossible parameters to characterize from crystallographic data, especially when the dopant is present at trace concentration levels. Given the significant role of scheelite-related materials in both environmental importance and technological innovation, an unambiguous revelation of actual local site symmetry in this family is necessary to optimize their performance for current and future applications.

Most structural studies focus on the effect of substitutions in the A position on the scheelite structure, especially in cases where the substitution is not charge commensurate, while much less attention has been paid to the impact of B site substitutions. Investigations have shown that the presence of excess positive charge in scheelite-type materials upon incorporation of a trivalent ion on the A site is compensated *via* coupled substitution with a monovalent alkali cation.[23-26] Other substitution schemes, such as two trivalent cations replacing three divalent A^{2+} ions plus a vacancy, could also be possible for imperfect structures.[27, 28] Single-crystal X-ray measurements demonstrate that the crystal structure of the resulting solid solutions is disordered, that is, the trivalent dopant and monovalent charge-compensating cation statistically occupy the same divalent A^{2+} site in ABO_4 structure.[29, 30] A theoretical study predicted a layered structure with alternating Na^+ and Ln^{3+} occupation in the A site using Monte Carlo simulations.[31] However, recent experimental studies found no evidence for a layered endmember of scheelite type solid solutions.[32, 33] An experimental study[34] of highly doped members of the general composition $Na_xEu^{3+}{}_{(2-x)/3}\Delta_{(1-2x)/3}MoO_4$ found evidence for structural ordering in some members of this solid solution series, but not the $NaEu(MoO_4)_2$ composition, using powder-XRD measurements. However, the ordering is explained by the formation of Eu^{3+} aggregates and not a layered structure. These aggregates, e.g. dimers, were shown to positively affect the luminescence properties of the materials, despite the well-known self-quenching effects in stoichiometric Eu^{3+} compounds.

In one previous endeavor to characterize the local site symmetry in a scheelite-related material, we characterized the solid solution series $Ca_{1.8}Na_{0.1}Gd_{0.1}(MoO_4)_8$ – $NaGd(MoO_4)_2$ co-doped with

Eu^{3+} in polycrystalline form, as well as a single crystal of the $NaGd(MoO_4)_2$ endmember by time-resolved laser-induced fluorescence spectroscopy (TRLFS).[32] The results revealed a deviation from the expected S_4 site symmetry that could be explained by relatively minor shifts in the guest cation's crystal field. It remained unclear, how the effect on the local structure translates to substitutions on the trace concentration level (i.e. well below 10% substitution, the lowest composition studied previously), which would e.g. be expected in a nuclear waste disposal scenario. Also, only one material from the scheelite family was investigated, so no information of the impact of the host cations on the guest cation environment could be obtained.

Here we focus on two aspects of the structural characterization of lanthanide-doped scheelite-type materials: the detailed characterization of the local coordination environment around Eu^{3+} dopants by polarization-dependent site-selective time resolved laser-induced fluorescence spectroscopy (p-TRLFS) and the effects of the A and B site cation on this local coordination environment. The p-TRLFS technique is unique in its capability to characterize the local environment of a fluorescent probe, here Eu^{3+}, in a multi-species system with point-group accuracy at trace concentration levels.[35] The optical properties of a luminescent Eu^{3+} center are largely governed by its local coordination environment, which is critically dependent on the crystal-field surrounding the emitter. This will improve our understanding regarding the formation of solid solutions on the molecular scale, and lead to an evaluation of the impact of lattice strain on the stability of the formed phase.

Materials and Methods

Crystal growth of scheelite-type ABO_4 ($A = Ca^{2+}, Sr^{2+}, Ba^{2+}$; $B = W^{6+}, Mo^{6+}$)

This crystals used in this work were grown by a high-temperature flux method, which is widely used to synthesize molybdate and tungstate crystals with desirable characteristics.[36, 37] The flux compositions and firing conditions are listed in **Table 1**. A nominal Eu-doping level of 500 ppm was chosen for each member in ABO_4 family. This doping level is sufficient for characterization by TRLFS, but is expected to have minimal impact on the host lattice structure.[8] For a typical experiment, the initial materials were thoroughly mixed in a mortar and packed into a Pt crucible. Europium was introduced by adding Eu_2O_3 powders into the mixture during the initial mixing stage. To ensure complete homogeneity, the mixture was heated to 50 °C above the holding temperature for a prolonged period as indicated in **Table 1**. The furnace temperature was then lowered to 650 °C at a rate of 3 °C/h followed by a quench. After each experiment, the resulting crystals were washed with boiling water to remove excess flux.

During crystal growth, it was found necessary to employ a slow cooling rate to guarantee growth of high-quality crystals. For example, a cooling rate below 5 °C/h yielded colorless translucent octahedral $CaWO_4$ crystals, up to 10 mm in size, with smooth (011) facets (see **Figure S1**), while flux inclusions were frequently observed for crystals grown with a cooling rate above 10 °C/h. In addition, high purity raw materials are essential to ensure consistent results, as the intensity of Eu^{3+} fluorescence is easily influenced by competitive energy transfer processes associated with small amounts (ppm and below) of impurity ions such as Fe^{3+}.

Table 1. The crystal growth conditions for single crystals used in this work.

Crystals	**Composition of starting materials (g)**	**Holding temperatures (°C)**	**Holding time (hours)**
$CaWO_4$	Na_2CO_3 (2.90), $CaCO_3$ (0.68), WO_3 (7.92), Eu_2O_3 (0.60 mg)	1070	5
$SrWO_4$	Na_2CO_3 (2.8), $SrCO_3$ (0.98), WO_3 (7.67), Eu_2O_3 (0.58 mg)	1070	5
$BaWO_4$	Na_2CO_3 (2.72), $Ba(NO_3)_2$ (1.67), WO_3 (7.43), Eu_2O_3 (0.56 mg)	1070	5
$NaEu(WO_4)_2$	Na_2CO_3 (1.5), WO_3 (7.9), Eu_2O_3 (1.2)	1000	5
$CaMoO_4$	Na_2CO_3 (4.14), $CaCO_3$ (0.98), MoO_3 (7.03), Eu_2O_3 (0.86 mg)	1050	2
$SrMoO_4$	Na_2CO_3 (3.96), $SrCO_3$ (1.38), MoO_3 (6.72), Eu_2O_3 (0.82 mg)	1050	2
$BaMoO_4$	Na_2CO_3 (3.78), $Ba(NO_3)_2$ (2.33), MoO_3 (6.42), Eu_2O_3 (0.79 mg)	1050	2
$NaEu(MoO_4)_2$	Na_2CO_3 (2.1), MoO_3 (7.1), Eu_2O_3 (1.7)	1000	2

Powder XRD Characterization and Single-Crystal Structure Analysis

The obtained crystals were characterized by X-ray diffraction. X-ray powder diffraction patterns were collected on a Rigaku MiniFlex diffractometer, equipped with a 600 W X-ray source tube ($\lambda = 1.54187$ Å) and a 6-position automatic sample changer. Data were recorded in the range of $2\theta = 10-80°$ with a step width of 0.02° and a counting time of 10 s/step, and analyzed using data given in the PDF-2 database. The X-ray powder diffraction patterns for all studied samples are provided in the Supporting Information (**Figure S2**). All samples can be unambiguously identified as the desired materials, and show no reflections not associated to the scheelite structure. No effect of doping with Eu^{3+} on the bulk crystal structure is observed, and consequently no information on the local coordination can be derived from the XRD data.

Crystals of as-grown Eu^{3+}- doped scheelite-type ABO_4 were analyzed on a Bruker D8 VENTURE diffractometer with a PHOTON 100 CMOS detector at room-temperature using microfocused Mo Kα radiation (λ = 0.71073 Å). Suitable single crystals were selected under a polarizing optical microscope and glued on a glass fiber for SC-XRD experiments. More than a hemisphere of data was collected for each crystal, and the three-dimensional data were reduced and filtered for statistical outliers using the APEX3 program. Data were corrected for Lorentz, polarization, absorption, and background effects. The SHELXL-97 program was used for determination and refinement of the structures.[38] The results of the single-crystal structural analysis show that the A site crystallizes exclusively in S_4 site symmetry in all the scheelite-type ABO_4 crystals.

Crystal Orientation

Scheelite belongs to the uniaxial crystals, which have only one optical axis, here the crystallographic *c*-axis; it is isotropic within the plane orthogonal to this axis. It is quite easy to identify the crystallographic *c*-axis for the as-grown crystals, since their sizes are big enough. **Figure S3** demonstrates the typical procedures needed to identity the optical axis for a $CaMoO_4$ crystal. First, the plane containing or perpendicular to the optical axis could be found with two crossed polarizers. After this, X-ray diffraction was carried out to check if the obtained optical axis is the crystallographic *c*-axis. In some cases, if the obtained crystal has natural faces, the optical axis can simply be determined through comparison of the faces with those of a simulated model, as shown in **Figure S1**.

Polarization-dependent Time Resolved Laser Fluorescence (p-TRLFS)

TRLFS was performed using a Nd:YAG laser system (Continuum) pumped dye laser (Radiant Dyes NarrowScan K). Rhodamine 6G was used as a dye for direct excitation of Eu^{3+} ions from the ground $^7F_0$ state to the emitting $^5D_0$ state (from 575 to 582 nm). The laser wavelength was monitored with a wavelength meter (High Finesse WS-5), and the laser energy was monitored using an optical power meter (Newport 1918-R). Luminescence signals were recorded from a spectrograph (Shamrock 303i) equipped with a polychromator with 300, 600 and 1200 lines/mm gratings and an intensified CCD detector (Andor iStar 734). Emission spectra, site-selective excitation as well as lifetime spectra were recorded at temperature below 10 K to obtain the spectral resolution required to discriminate different crystal-field transition lines of Eu^{3+}. Before the measurement, the grating was calibrated from the emission lines of a neon lamp. In order to minimize the effect of the laser pulse on the spectra, the minimum gate delay between laser pulse and camera gating was set to 1.0 μs. The gate width of the camera was fixed at 10 ms to ensure the collection of the entire fluorescence signal.

The fluorescence signals were recorded along two polarization directions, namely, σ and π, relative to the crystal's optical axis. **Figure 1** shows the setup of the π-polarized fluorescence experiment. The excitation laser beam emitted from the dye laser is polarized with its electric vector (***E***) parallel to the direction of the z-axis, shown in **Figure 1**. The polarized beam is monitored by a polarizer (Glan-Laser Calcite Polarizer) and then reflected at a right angle by a prism. After turning, the incident light propagates along the z-axis with its electric vector parallel to the x-axis. Spectra were recorded with light propagating transverse to the crystallographic *c*-axis of each crystal sample. The π spectrum is determined with the ***E*** vector parallel to the *c*-axis, whereas the σ spectrum is defined by ***E*** perpendicular to the *c*-axis. For the lifetime measurement, no polarized spectra were recorded.

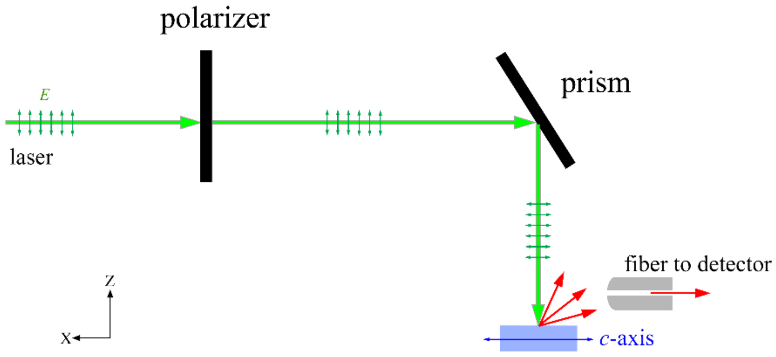

Figure 1. The setup used for polarized TRLFS measurements. This figure demonstrates π-polarization geometry where the optical axis (the crystallographic *c*-axis is parallel to the electric vector)

Site symmetry of dopants and TRLFS

The crystal structure of undisturbed ABO_4 can be seen as derived from the CaF_2 fluorite in which the alkaline-earth A^{2+} ions occupy position 4*a*, hexavalent Mo^{6+}/W^{6+} on position 4*b* and O^{2-} on position 16*f*, respectively.[39] The replaceable A^{2+} ions are located at a site with a crystallographic point symmetry of S_4: Each A^{2+} ion has 8 O^{2-} ions in its first coordination sphere, and its second coordination sphere consists of 4 A^{2+} and 8 B^{6+}. Trivalent lanthanide ions can be introduced into such a host in the geometry of a LnO_8 square antiprism by replacing A^{2+} ions. The charge and radius differences between dopant and host cations generally results in a number of local structural distortions that makes any X-ray structural determination tedious or even impossible. Therefore, the study of the luminescence of the dopant ion can be very useful.

When the luminescent probe Eu^{3+} ion is introduced, it enters the crystal lattice accompanied by a charge-compensating Na^+ cation to randomly substitute for divalent A^{2+} sites,[26] leaving it in a crystalline environment where the most important crystal-field contribution originating from the 8 nearest-neighbor O^{2-} ions. Due to the mismatch of ionic radius and electric charge between the Eu^{3+} and A^{2+} cations, the bond length of Eu-O will undoubtedly be different from the original A-O bond length, which thus disturbs the coordination shell around the 4*a* site. As a result, the crystal-field environment around the Eu^{3+} dopant will be perturbed, and the local site symmetry of Eu^{3+} may be altered from S_4 to lower symmetries, such as C_{2v}, C_2, or even C_1, depending on the displacement patterns of the 8 O^{2-} in the first coordination sphere around these Eu^{3+} centers. The extent of this change in bond length will depend strongly on the size difference between host and guest cation, as well as the flexibility of the crystal lattice.

The details of the Eu^{3+} environment in crystalline structures can be obtained from the combined excitation ($^5D_0 \leftarrow {}^7F_0$) and fluorescence emission ($^5D_0 \rightarrow {}^7F_J$, J = 1, 2) spectra. Eu^{3+} TRLFS is a versatile tool that can respond to small structural differences for a luminescent center in solids, solutions and at the interface.[40-42] Eu^{3+} is considered the most extensively used spectroscopic probe, attributable to its high sensitivity and relatively simple luminescence spectrum. The use of optical spectra of Eu^{3+} in solving complex problems in solid-state chemistry has been studied extensively and reviewed thoroughly.[26, 43, 44]

Excitation spectra are obtained by integrating the fluorescence intensity as a function of the excitation wavelength. Therefore, the resolution is not limited by the resolution of the detector but only by the tuning resolution of the laser system (< 0.01 nm). For the excitation from the $^7F_0$ ground state to the $^5D_0$ state, a single line is observed, due to the fact that both $^7F_0$ and $^5D_0$ states are non-degenerate. Whenever several lines are observed for the $^5D_0 \leftarrow {}^7F_0$ transition, Eu^{3+} ions are situated in sites with different local environments (different species). The number of the $^5D_0 \leftarrow {}^7F_0$ transition lines in the excitation spectra is then the number of non-equivalent Eu^{3+} species. Furthermore, selective excitation of each of the Eu^{3+} species to the $^5D_0$ state by a tunable laser yields fluorescence emission spectra of each single species. The splitting patterns of the $^5D_0 \rightarrow {}^7F_1$ and $^5D_0 \rightarrow {}^7F_2$ transitions give information on the site symmetry of the Eu^{3+} ions. This is because the $^5D_0$ ground state is non-degenerate, so that any observed splitting is the consequence of the lifting of the degeneracy of the $^7F_1$ and $^7F_2$ sublevels. The extent to which the degeneracy of $^7F_1$ and $^7F_2$ sublevels is reduced depends on the crystal-field perturbation on the luminescent Eu^{3+} ions.[44]

Moreover, the use of polarized light can provide site symmetry information that is difficult or impossible to obtain by other spectroscopic techniques. In general, the crystals are distinguished as being either isotropic or anisotropic based on whether or not their three crystallographic axes are equivalent. Isotropic crystals axes' are symmetry equivalent, and the crystal will interact with light equally, regardless of the sample orientation with respect to incident light waves. On the contrary, anisotropic crystals have crystallographically distinct axes and interact with light non-uniformly. For a uniaxial crystal like scheelite, where two out of the three crystallographic axes are interchangeable, light still behaves isotropically when propagating along the optical axis (the non-interchangeable axis, here the *c*-axis), but the observed transitions and splitting patterns will be affected when light propagates in any other direction. This is due to the fact that a transition is permitted only in certain direction while it is forbidden in other directions.[44] Depending on the orientation of the crystal lattice with respect to the incident light's polarization plane, the observed anisotropic emission effects vary between two extreme situations, with the directions of the light's electric vector perpendicular (σ polarization) or parallel (π polarization) to the crystallographic-*c* axis. With the aid of the selection rules, the polarization characteristics of emission lines which originate from transitions between different crystal-field levels of the Eu^{3+} ions can be used to deduce the local site symmetry.[45]

Results and Discussion

The influence of A and B sites on the species of Eu^{3+} dopants in ABO_4 scheelite-related hosts

Figure 2 shows the excitation spectra of the Eu^{3+} ($^5D_0 \leftarrow {}^7F_0$) transition between 575 nm and 582 nm (17391 cm^{-1} – 17182 cm^{-1}) of all members in Eu^{3+} doped ABO_4 (A = Ca^{2+}, Sr^{2+}, Ba^{2+}; B = W^{6+}, Mo^{6+}) family together with the two endmembers $NaEu(WO_4)_2$ and $NaEu(MoO_4)_2$. The spectral profiles of the tungstates are almost identical with their molybdate counterparts, and all eight spectra can be roughly divided into two parts, (i) a higher wavelength (or lower energy) range between 578 nm and 581 nm (17301 cm^{-1} – 17212 cm^{-1}) where one narrow well-resolved peak with a full width at half maximum (FWHM) in the range of 1-16 cm^{-1} can be found for every sample and (ii) a second part at shorter wavelength (higher energy) from 575 nm to 577 nm (17391 cm^{-1} – 17331 cm^{-1}), which shows a broad feature for all spectra, except for the Ca-based materials $CaWO_4$ and $CaMoO_4$. Both of these show a sharp transition located at 578.4 nm (17289 cm^{-1}).

A similar situation has been observed in our previous Eu^{3+} TRLFS studies of Gd^{3+} incorporated powellite solid solutions, where it was concluded that the broad signals in the lower-wavelength range are not from a separate species but arise from a "hot band" of the major species, based on the observation that the same emission spectrum was observed independent of the excitation energy.[32] The peak is likely related to an energy transfer process involving Mo, so "energy transfer band" would be a more appropriate designation. For our samples, fluorescence emission spectra recorded with both excitation energies are clearly different, indicating that two incorporated Eu^{3+} species are present in $CaMoO_4$ and $CaWO_4$. The site distribution of incorporated Eu^{3+} is more complicated than expected. For the sake of the following discussion, the species appearing in the low and high wavelength ranges for the excitation spectra of $CaWO_4$ and $CaMoO_4$ are assigned as X and Y, respectively (see **Figure 2**). Detailed polarization-dependent fluorescence spectra will be discussed in the following section.

In the case of species Y, a trend of linewidth broadening can be noted across both the molybdate and tungstate series with increasing host cation radius. It is obvious that the linewidth increases with the degree of incompatibility between host and dopant cation radii. **Table 2** lists the respective cation radii and the associated FWHM of the $^5D_0 \leftarrow {}^7F_0$ transitions. As is shown in this table, the ionic radius of the host cation in the scheelite-type structures increases systematically from Ca^{2+} (r = 1.12 Å), through Sr^{2+} (r = 1.26 Å), toward Ba^{2+} (r = 1.42 Å) by ≈ 27%.[16] $CaWO_4$ and $CaMoO_4$ with a host cation radius similar to Eu^{3+} dopant (1.07 Å)[16] have the narrowest FWHM of 1 and 3 cm^{-1}, respectively; whereas the widest FWHM of 6 and 9 cm^{-1} are found in $BaWO_4$ and $BaMoO_4$, respectively. A similar trend was previously observed in a Eu^{3+} doped $LaPO_4$–$GdPO_4$ monazite solid solution series.[20]

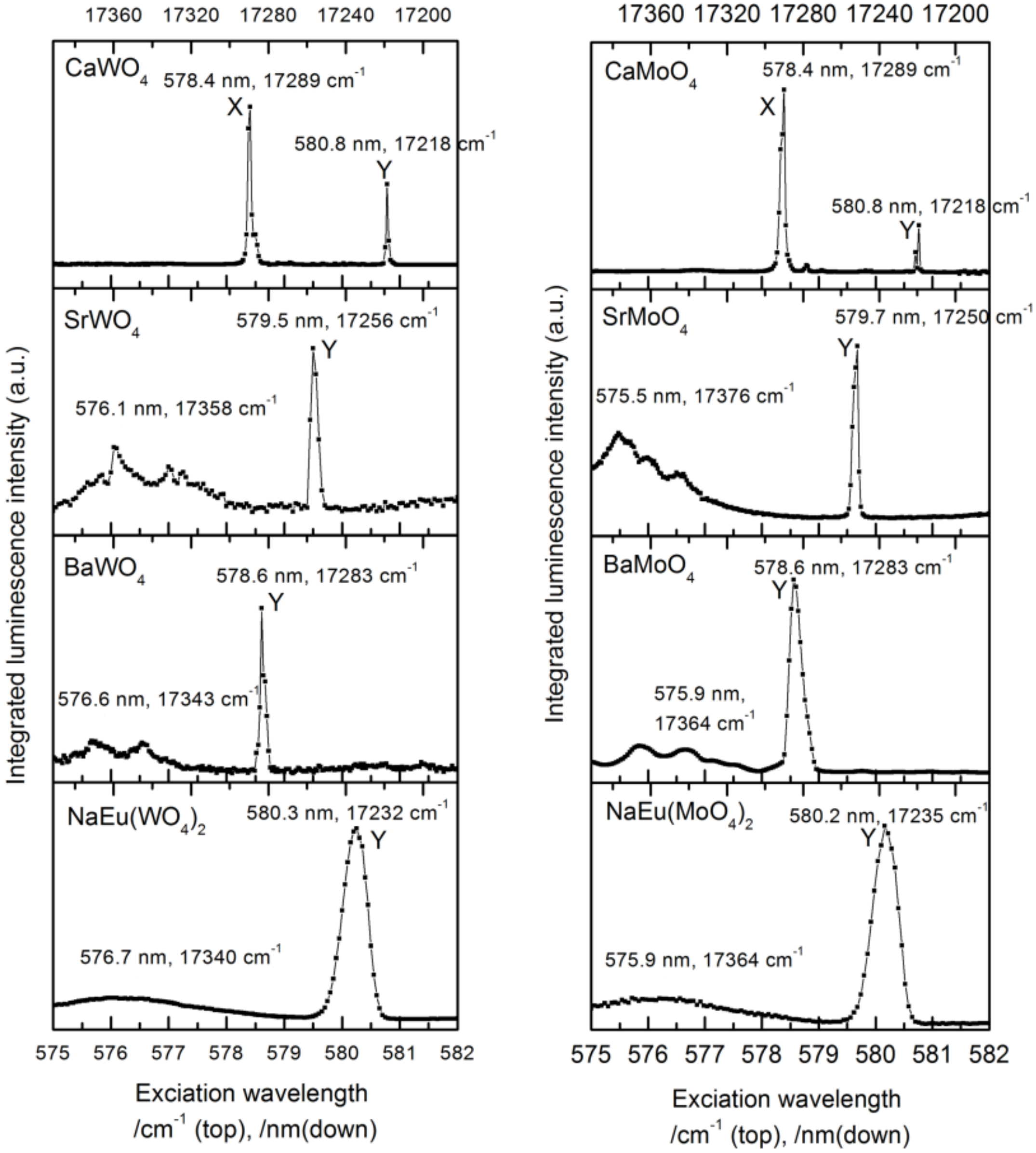

(a) (b)

Figure 2. Excitation spectra of the Eu^{3+} ($^5D_0 \leftarrow {}^7F_0$) between 575 and 582 nm of all members in Eu^{3+} doped ABO_4 (A = Ca^{2+}, Sr^{2+}, Ba^{2+}; B = $W^{6+,}$ Mo^{6+}) family together with the two end-members of $NaEu(WO_4)_2$ and $NaEu(MoO_4)_2$.

Table 2. Comparison between cation radius and the associated FWHM of the $^5D_0 \leftarrow {}^7F_0$ transitions

	Ion size	**Excitation max. species Y**	
Crystals	**(Å)**	**location (nm)**	**FWHM (nm)**
$CaWO_4$	1.12	580.9	0.05
$SrWO_4$	1.26	579.5	0.13
$BaWO_4$	1.42	578.6	0.13
$NaEu(WO_4)_2$	1.18	580.3	0.57
$CaMoO_4$	1.12	580.8	0.04
$SrMoO_4$	1.26	579.7	0.12
$BaMoO_4$	1.42	578.6	0.29
$NaEu(MoO_4)_2$	1.18	580.2	0.53

It is noteworthy that the broadening is most pronounced in the endmembers, that is, 16 cm^{-1} for $NaEu(WO_4)_2$ and 14 cm^{-1} for $NaEu(MoO_4)_2$, respectively. **Figure 3** illustrates the substantially broader excitation peak of $^5D_0 \leftarrow {}^7F_0$ transition in $NaEu(WO_4)_2$. A similar increase for the $NaEu(MoO_4)_2$ endmember (17 cm^{-1}), relative to samples with lower degree of doping (8 cm^{-1} at 10% substitution) was reported in our earlier work.[32] The increased line-broadening must be related to the random distribution of Na^+ and Eu^{3+} over the A lattice sites and the resulting structural disorder in the $NaEu(BO_4)_2$ materials. This structural disorder would exert slightly different crystal-fields for every specific Eu^{3+} (and Na^{+}) dopant. In this regard, the Eu^{3+} ions are distributed over several very similar but not identical lattice sites, that is, a continuum of Eu^{3+} environments.[44] This line-broadening phenomenon is more profoundly observed in structural fully disordered glasses. It is reported that, the $^5D_0 \leftarrow {}^7F_0$ transitions are composed of nearly 50 slightly different C_s site symmetries in phosphate glasses, leading to a FWHM of almost 119 cm^{-1}.[46, 47] In fact, the mechanism of spectral linewidth broadening for trivalent lanthanides induced by the structural disorder has long been applied to increase the performance of tunable solid-state laser operation.[48, 49]

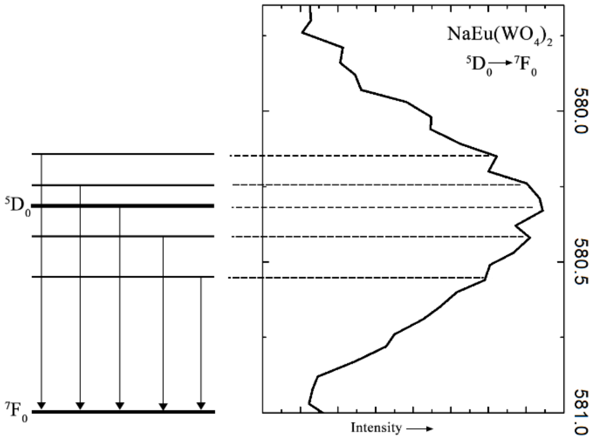

Figure 3. An inhomogeneous line broadening of the $^5D_0$ – $^7F_0$ transition which consists of subsets of transitions between different $^{2S+1}L_J$ multiplets shows a continuum of Eu^{3+} environments.

The peak position of the excitation band allows for an estimate of the strength of the crystal field each Eu^{3+} species experiences. Stronger coordination leads to larger crystal field splitting and thus lower energy transition, i.e. a bathochromic shift of the signal. As shown in **Figure 2**, the excitation maxima for both the molybdate and tungstate family shifts to lower wavelength, as the ionic radii of the host cation increases from Ca^{2+} to Ba^{2+}. This decrease in the excitation wavelength is related to the reduced strength of the coordinative bond from O atoms at larger distances.[50] The blue shift follows a linear trend, and the excitation energy can be expressed as a linear function (f(x) = a + b*x*) of both, the radius of the host cation (eqs. 1a, 2a) and the A—O bond distance (eqs. 1b, 2b). The results of the linear fit to the experimental data are shown in **Figure 4**, and the resulting equations for the tungstate and molybdate compounds are shown in equation (1) and (2), respectively.

Tungstates: $X_c(^5D_0 \leftarrow {}^7F_0)\ [\mathrm{cm^{-1}}] = 16975 + 218R_A[\text{Å}]$ (1a)

$X_c(^5D_0 \leftarrow {}^7F_0)\ [\mathrm{cm^{-1}}] = 16597 + 253r_{A-O}\ [\text{Å}]$ (1b)

Molybdates: $X_c(^5D_0 \leftarrow {}^7F_0)\ [\mathrm{cm^{-1}}] = 16981 + 213R_A[\text{Å}]$ (2a)

$X_c(^5D_0 \leftarrow {}^7F_0)\ [\mathrm{cm^{-1}}] = 16578 + 259r_{A-O}\ [\text{Å}]$ (2b)

where X_c and R_A and r_{A-O} stand for excitation energy and host cation radius and average A-O bond distance, respectively. The small differences of a few cm^{-1} between tungstates and molybdates shows that the observed effects are not associated with differences of the B site cations in the ABO_4 family. A linear trend with the crystallographic A – O bond is a strong indicator that the distortion upon substitution of Eu^{3+} for M^{2+} is minor. The same linear trend has recently been observed for Eu^{3+}-doped monazites $LnPO_4$, which are a much better structural fit for Eu^{3+} than especially the Sr^{2+} and Ba^{2+} compounds studied here.[20] Huittinen et al. find parameters of a = 17053 cm^{-1} and b = 194 $(cm\times\text{Å})^{-1}$ in good agreement with the parameters obtained here, despite the structural and compositional differences between the monazites $LnPO_4$ and the scheelite-type materials ABO_4.

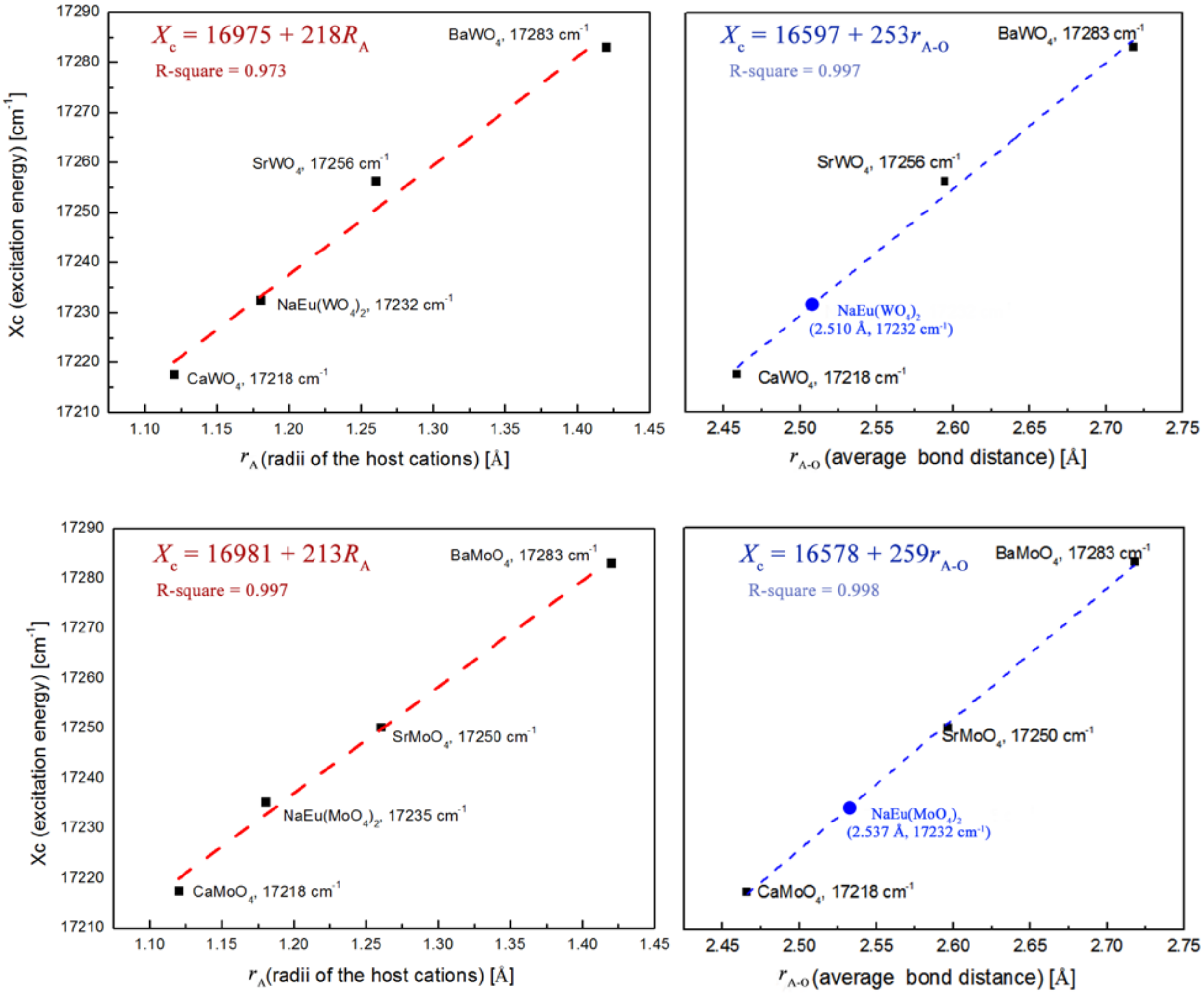

Figure 4. The linear trend of the excitation energy X_c (cm^{-1}) changes as a function of the host cation radius r (Å) and average bond distance $r_{A\text{-}O}$ (Å) in Eu^{3+} doped scheelite-typed materials. (left) Excitation energy changes against the host radius in scheelite series. (right) Excitation energy changes against the host radius in powellite series.

The derived equations can be used to obtain the Eu – O bond distance in the randomly distributed $NaEu(BO_4)_2$ endmembers. This is especially important for the case of $NaEu(WO_4)_2$, since there is no single crystal data available for this compound. Using equation 1b and 2b, a value of 2.537 Å for $NaEu(MoO_4)_2$ and a slightly shorter bond distance of 2.510 Å for $NaEu(WO_4)_2$ could be calculated, respectively. The obtained Eu – O bond distance in $NaEu(MoO_4)_2$ is larger than that of a monoclinic polymorph (2.4601 Å), which had been deduced from Rietveld refinement using (3+1)-dimension symmetry and the Eu^{3+} has the site symmetry of C_2.[2]

Breakdown of crystallographic site symmetry in ABO_4

To examine the local structural details of the species in ABO_4 single crystals, fluorescence emission spectra for each identified species were recorded in σ and π polarization geometry. For most species, the polarization dependency is weak, and the symmetry can be assigned based on the emission spectrum with arbitrary polarization. So far, the only p-TRLFS experiments in this system were carried out with $NaGd(Eu)(MoO_4)_2$, hence, we will begin the discussion with the other endmember of this series $Ca(Eu)MoO_4$, which shall also serve as a reference for the subsequent discussion.

$CaMoO_4$

Two sharp peaks at 578.4 nm (17289 cm^{-1}) and 580.8 nm (17218 cm^{-1}), corresponding to species X and Y, can be identified for $CaMoO_4$ excitation spectra (**Figure 2 (b)**). In the other endmember $NaEu(MoO_4)_2$, only one species with an excitation wavelength of 580.3 nm

(17232 cm^{-1}) had been identified, along with a weak “energy transfer band” at ~576 nm (17361 cm^{-1}). A red-shift of the $^5D_0 \leftarrow {}^7F_0$ transition for lower degrees of substitution had already been noted in the previous study as well.[32]

When species Y is excited selectively at 580.8 nm (17218 cm^{-1}) **Figure 5 (b)**), the emission spectrum exhibits one peak assigned to the $^5D_0 \rightarrow {}^7F_0$ transition and a mono-exponential luminescence decay behavior, confirming that a single species was excited. The transitions ($^5D_0 \rightarrow {}^7F_1$) and ($^5D_0 \rightarrow {}^7F_2$) split into three and four lines, respectively, with no dependence on the polarization direction of the laser, which indicates the symmetry around the Eu^{3+} ions is C_{2v}.[51] The intensity ratio of the ($^5D_0 \rightarrow {}^7F_1$)- to the ($^5D_0 \rightarrow {}^7F_2$)-transitions is very small at 0.10, in good agreement to the ratio of 0.11 reported previously.[32] Excitation of species X at 578.4 nm (17289 cm^{-1}) (**Figure 5 (a)**), also shows one peak for the $^5D_0 \rightarrow {}^7F_0$ transition. This means the existence of only one species for the Eu^{3+} ions, which is also in agreement with the mono-exponential decay behavior in the luminescence decay curves of the emitting $^5D_0$ level. The number of identified $^5D_0 \rightarrow {}^7F_J$ transitions is one, three and four for $J = 0$, 1 and 2, respectively, suggesting a C_{2v} symmetry also for species X.

Even though the emission spectra of species X and Y show very similar splitting patterns, there are differences in the details of the spectral profiles, concerning both the relative intensities of J-sublevel transitions and the overall ratio of ($^5D_0 \rightarrow {}^7F_1$)- to the ($^5D_0 \rightarrow {}^7F_2$)-transition, which is significantly larger for species X with a value of 0.21. For example, for species X, the $^5D_0 \rightarrow {}^7F_2$ band is separated into one strong and three weaker lines, whereas for species Y, two strong and two weak lines comprise the same F_2 band. Besides, for species X, the three peaks in the F_1 band are located widely distributed from 584 – 597 nm (17123-16750 cm^{-1}), but those observed for species Y are found within 591 – 596 nm (16920-16779 cm^{-1}). Based on these observations, it is safe to conclude that Eu^{3+} doped $CaMoO_4$ contains two unique species, both of which show C_{2v} symmetry, but with obvious differences in the specific arrangement of the crystal field.

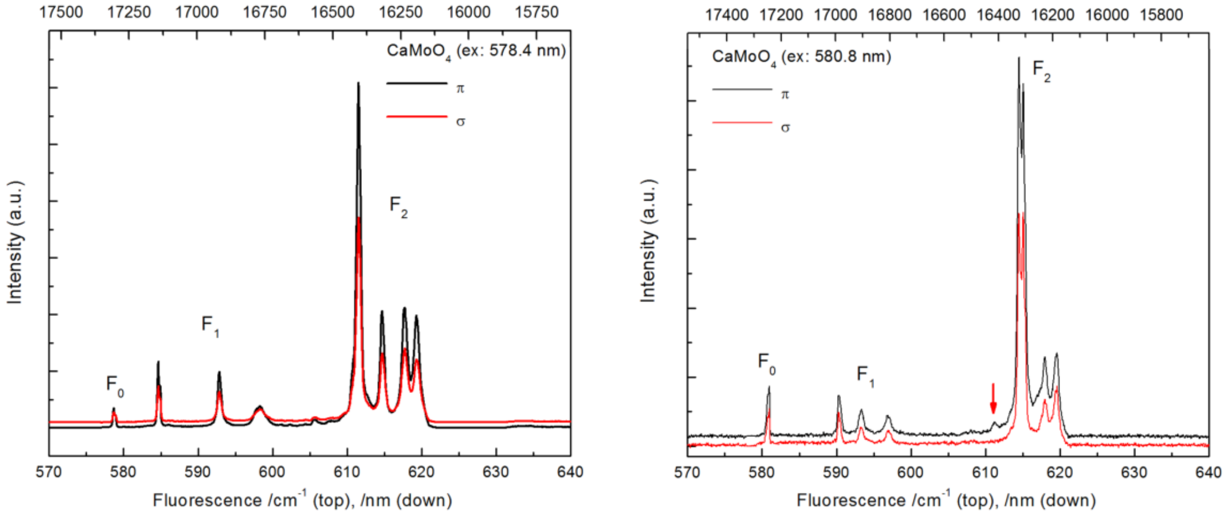

(a) (b)

Figure 5. Fluorescence emission of Eu^{3+} doped $CaMoO_4$ under (a) 578.4 nm (17289 cm^{-1}) and (b) 580.8 nm (17218 cm^{-1}) excitation.

$CaWO_4$

As discussed for $CaMoO_4$, two sharp peaks – one at low energy of 578.4 nm (17289 cm^{-1}) and the other at higher energy of 580.8 nm (17218 cm^{-1}) – appear in the excitation spectrum of Eu^{3+}-doped $CaWO_4$ (see **Figure 2 (a)**), at the same wavelengths as discussed for $CaMoO_4$. To ascertain whether these two peaks can be assigned to the same Eu^{3+} species, and to characterize their local coordination geometry the respective polarized fluorescence emission spectra after site selective excitation were obtained (**Figure 6**).

After excitation at 580.8 nm (17218 cm^{-1}) (**Figure 6 (b)**), the emission spectrum with σ polarization geometry is nearly identical to the one observed for $CaMoO_4$, indicating that this species must be similar or equivalent to species Y of $CaMoO_4$. However, unlike in powellite, the luminescence of species Y in scheelite shows a pronounced dependence on the polarization geometry. In π geometry, the splitting in the F_1 band is reduced from three to two, while the two highest energy lines of the F_2 band, which are near degenerate in σ geometry, are clearly separated and exhibit different intensities in π geometry. Total numbers of (1σ, 1π), (3σ, 2π) and (4σ, 4π) transition lines for F_0, F_1 and F_2 transitions are observed.

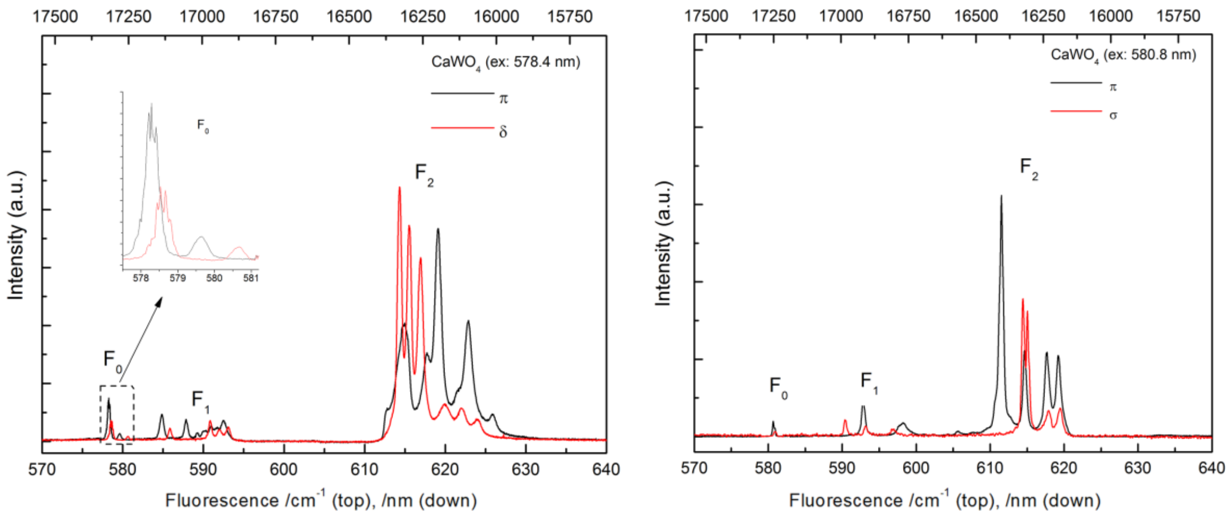

(a) (b)

Figure 6. Fluorescence emission of Eu^{3+} doped $CaWO_4$ under (a) 578.4 nm (17289 cm^{-1}) and (b) 580.8 nm (17218 cm^{-1}) excitation.

The interpretation of these patterns is, however, not trivial. Ideally, the Eu^{3+} ions replacing Ca^{2+} in crystalline $CaWO_4$ should be located at a crystallographic site with symmetry of S_4. In this perspective, however, it is clear that the observed transition lines for species Y in scheelite cannot match S_4 symmetry, as the S_4 symmetry would produce only (1σ, 2π) peaks for $^5D_0 \rightarrow {}^7F_2$ transition (**Figure S4**). Clearly, species Y experiences a crystal field of lower symmetry. The spectrum obtained in σ polarization geometry, as well as those with arbitrary polarization, point to a C_{2v} symmetry, as discussed for species Y in powellite. But, as also discussed previously, C_{2v} point symmetry should not exhibit any polarization dependence, which is clearly not the case here. Taken together, it seems reasonable to conclude that the actual local symmetry around Eu^{3+} on site Y is a combination of S_4 and C_{2v}, in such a way that the distortion in the lattice is so minor that a residual character of the crystallographic high symmetry site is retained, but still strong enough to affect the Eu^{3+} luminescence. A second possible explanation could be that the randomly distributed nature of incorporated Eu^{3+} in the resulting solid solution, leads to a situation where part of the Eu^{3+} ions may reside in virtually undisturbed host sites retaining S_4 symmetry, while other parts of the Eu^{3+} ions are distributed at distorted sites with C_{2v} symmetry. It is then, however, unclear why both site symmetries produce only one peak in the excitation spectrum. In either case, it is obvious that relative to the isostructural $CaMoO_4$ phase, the $CaWO_4$ lattice has undergone less distortion to accommodate Eu^{3+}.

In the case of the species with the higher excitation energy of 578.4 nm (17289 cm^{-1}) (**Figure 6 (a)**), the emission spectra also show strong dependence on the polarization geometry. Specific interpretation is complicated by the fact that evidently two species are excited simultaneously. The F_0 area is seen to consist of two adjacent lines in both σ and π polarization directions. As shown in the inset of **Figure 6 (a)** the two lines correspond well with the excitation spectrum shown in **Figure 2 (a)** for σ geometry, meaning it is likely that there is an energy transfer mechanism from the high energy species X to the lower energy species Y. A possible mechanism could be the existence of an "energy transfer band" of species Y, as was observed previously,[32] which overlaps with the excitation peak of species X, which is seen as a broad and structured band in the spectra. Evidence for the existence of such bands in the Sr and Ba compounds will be discussed in the next section. Unfortunately, this lead to an overlap in the emission spectra, and our attempts to delineate the single species spectra were unsuccessful. As the number of bands observed exceeds the maximum number of *J*-sublevels (2J + 1) an interpretation of the site symmetry is not applicable. Nevertheless, it should be noted that both the F_1 and the F_2 band show a distinct dependence on the laser's polarization plane, which cannot be explained with an overlap with the emission of species Y alone (e.g. comparing the low energy lines within the F_2 band). This indicates that also for species X less lattice distortion was induced by the substitution of Eu^{3+} for Ca^{2+} in $CaWO_4$ than in $CaMoO_4$.

Other scheelite-typed crystals

Figure 7 shows the fluorescence emission spectra of species Y for the remaining six crystals ($SrWO_4$, $SrMoO_4$, $BaWO_4$, $BaMoO_4$, $NaEu(WO_4)_2$ and $NaEu(MoO_4)_2$). Excitation within the broad excitation features at lower wavelength yields the same emission spectra as direct excitation of species Y. This indicates that for these materials species X is absent, while the excitation at lower wavelength and thus higher energy, can be attributed to the "energy transfer band" effect for these six crystals.

A comparison of the emission spectra of $SrWO_4$ and $SrMoO_4$, at first sight, indicates a close similarity in terms of profile and splitting patterns. Both spectra have one line in the $^5D_0 \rightarrow {}^7F_0$ transition and two lines in the $^5D_0 \rightarrow {}^7F_1$ transition. Since the sublevels of the F_1 band in these two spectra are very broad and have relatively low intensity, the exact number of lines for the F_1 band may however not be resolved. A minor effect of the polarization on the F_2 band can be observed upon close inspection of the spectrum of $SrWO_4$. That is, in π-geometry, the F_2 band is fourfold split, while in σ-geometry the peak at 618 nm disappears and a threefold splitting is found. A similar effect may exist for $SrMoO_4$, but the line is overall weaker and broader making a clear distinction impossible. This again indicates a lesser distortion of the crystal lattice for W-based $SrWO_4$ than for Mo-based $SrMoO_4$.

In the case of Ba-based $BaWO_4$ and $BaMoO_4$, both spectra have transition lines of (1σ, 1π), (3σ, 3π) and (4σ, 4π) for the $^5D_0 \rightarrow {}^7F_{0,1,2}$ transitions, respectively, which is in agreement with that predicted by the selection rules for Eu^{3+} in a C_{2v} site. However, obvious differences could be seen between the spectra of the tungstate and the molybdate. In particular, it is clear that the fourfold F_2 band is better resolved in $BaMoO_4$ than in $BaWO_4$ (see **Figure 7**). In $BaWO_4$, the fourfold splitting of the F_2 band is composed of two strong and two relative low peaks, whereas the $BaMoO_4$ exhibits one strong and three low intensive peaks. In other words, while the point symmetry is identical in both materials the specific arrangement of the O ligands differs.

The emission spectra of both $NaEu(WO_4)_2$ and $NaEu(MoO_4)_2$ are very similar to those observed in Eu^{3+} doped $NaGd(MoO_4)_2$.[32] In all these three crystals, the numbers of crystal-field transition lines from $^5D_0$ to $^7F_0$, $^7F_1$ and $^7F_2$ are one, three, and four, respectively. The splitting patterns confirm the earlier finding that the Eu^{3+} ions in these crystals exclusively occupy a C_{2v} site symmetry. The fact that the local coordination environment in these materials shows no dependence on the B site cation, could suggest that site symmetry of the incorporated Eu^{3+} and the distortion of the crystal lattice is controlled by the statistical distribution of the A site cations Na^+ and Eu^{3+} in these materials, and the B site cation has less influence on the local distortion.

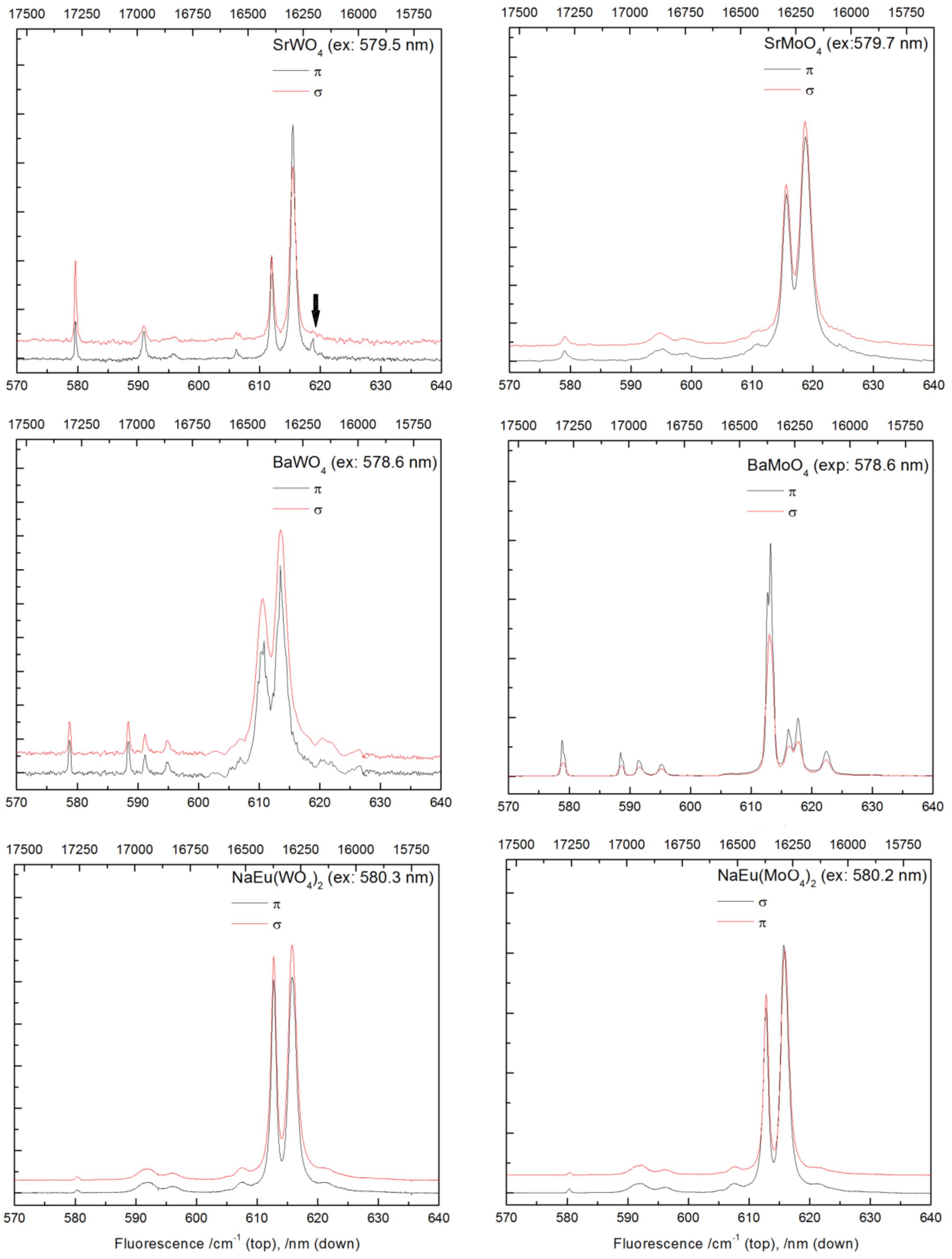

Figure 7. The fluorescence spectra under high wavelength excitation for SrWO$_4$, SrMoO$_4$, BaWO$_4$, BaMoO$_4$, NaEu(WO$_4$)$_2$ and NaEu(MoO$_4$)$_2$, respectively. The black arrow in SrWO$_4$ indicates the minor effect of polarization in F$_2$ band.

Conclusions

In ideal ABO_4 single-crystals, it is observed that the A^{2+} ions are located in a tetragonal crystallographic site symmetry (S_4). It is therefore often assumed that this is only dopant site in a resulting solid solution as long as the differences in ionic radii between host and guest is sufficiently small. Our polarization-dependent TRLFS results with Eu^{3+} as a structural probe reveal that that the speciation of the incorporated Eu^{3+} is much more complicated than expected. In particular, the effect of the B site cation is significantly more pronounced than previously assumed. The crystal-field surrounding the A^{2+} site is mainly contributed by the eight nearest-neighbor oxygen atoms. A minor distortion of this crystal-field, for instance, any concerted displacement of any two oxygen atoms would result in the loss of the mirror plane perpendicular to the S_4 axis and lead to a site with C_{2v} point symmetry (**Figure 8**). Our experimental results show that in addition intermediates may form between these two-point symmetries that are less symmetrical than the crystallographic site, but more symmetrical than the distorted C_{2v} point symmetry.

The specific distortion of the lattice depends on both the A and B cations. With the increase of the A^{2+} host cation radius and A-O bond distance from Ca^{2+} to Ba^{2+}, we observe a line-broadening trend across the ABO_4 family, which arises from multiple similar cationic environments introduced by the coupled substitution. This broadening feature is most pronounced in the endmembers $NaEu(WO_4)_2$ and $NaEu(MoO_4)_2$ due to the extremely heterogeneous coordination environments surrounding the Eu^{3+} ions. Second, the position of high wavelength excitation peaks shows a remarkable linear dependence upon host cation radius. The fact that the $^5D_0 \leftarrow {}^7F_0$ band shift to higher energy (blue shift) with the increase of the host cation radius indicates a weaker metal-ligand interaction, showing that the oxygen atoms within the lattice do not deviate strongly from their crystallographic positions and Eu-O bond distances are mostly governed by the bond distance of A to oxygen in the structure. The linear correlation between the excitation energy of the $^5D_0 \leftarrow {}^7F_0$ transition and the average Eu – O bond distance could be used to calculate average bond distances for the $NaEu(BO_4)_2$ compounds that are not readily available in the literature. We find values of 2.537 Å for $NaEu(MoO_4)_2$ and 2.510 Å for $NaEu(WO_4)_2$, which fall in between the values of the Ca^{2+} and Sr^{2+} compounds, and are significantly larger than the value previously reported for $NaEu(MoO_4)_2$.[34]

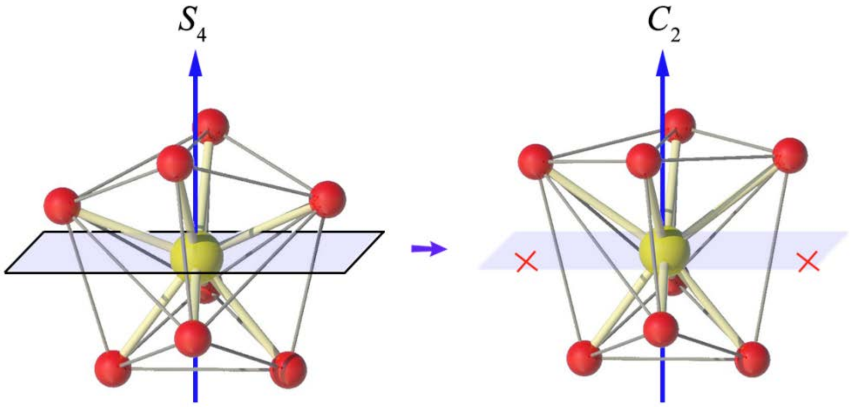

Figure 8. Schematic representation of the breakdown of crystallographic site symmetry of Eu^{3+} ions in scheelite-based ABO_4 (A = Ca^{2+}, Sr^{2+}, Ba^{2+}; B = W^{6+}, Mo^{6+}) materials. Left, the crystallographic S_4 symmetry, right, the most common distortion to C_{2v}. Legend: red and yellow spheres stand for O and Eu, respectively.

The role of the B cation on the doping site symmetry is less straightforward. The ions of Mo^{6+} and W^{6+} have near equal radii and the same tetrahedral coordination geometries, therefore the incorporation of trivalent ions on the A site for either tungstate or molybdate would be expected to not be affected by the occupation of the B site. However, we observe a general trend that the tungstates in the ABO_4 family exhibit higher symmetry environments for the Eu^{3+} dopant. This is seen most clearly in the $CaBO_4$ materials, where only C_{2v} site symmetry is observed for both species in $CaMoO_4$, but a higher symmetry character is preserved for the same species in $CaWO_4$. A similar trend is also observed for the Sr-based tungstate and molybdate compounds, with $SrWO_4$ showing slightly stronger polarization dependency than $SrMoO_4$. A recent crystallographic study found that WO_4^{2-} is more rigid with respect to stretching of the M – O bond than MoO_4^{2-}, but is more easily capable to accommodate dopants by rotational displacements.[33] This would indicate that the rotational displacement preferred by the WO_4^{2-} units leads to a local environment for the Eu^{3+} guest cation that is less distorted from its crystallographic symmetry. Similar effect has also been previously observed in a series of scheelite-type isostructural tungstate and molybdate compounds.[52]

In summary, we have demonstrated that a detailed understanding of doped solid-state materials must rely on the characterization of local structural effects, and that p-TRLFS with appropriate luminescent probes is an excellent tool for such atomic level characterization. Only this atomic level understanding is suited to take on such diverse problems as tailoring new materials for specialized applications and predicting the stability of secondary phases over the long time scales required for nuclear waste disposal.

ASSOCIATED CONTENT

Supporting Information.

Additional figures and tables providing PXRD data, single crystal face orientation steps and selection rules used for site symmetry determination of Eu^{3+} luminescence. (PDF)

AUTHOR INFORMATION

Corresponding Author

*E-mails: moritz.schmidt@hzdr.de

Author Contributions

The manuscript was written through contributions of all authors.

Notes

The authors declare no competing financial interest.

ACKNOWLEDGMENT

We gratefully acknowledge the Helmholtz Gemeinschaft Deutscher Forschungszentren for supporting the Helmholtz-Nachwuchsgruppe “Structures and Reactivity at the Water/Mineral Interface” (VH-NG-942). We thank Nina Huittinen and Thorsten Stumpf for discussion and help.

REFERENCES

(1) Brugger, J.; Giere, R.; Grobeéty, B.; Uspensky, E., *Am. Mineral.* **1998,** *83*, 1100-1110.

(2) Arakcheeva, A.; Logvinovich, D.; Chapuis, G.; Morozov, V.; Eliseeva, S. V.; Bünzli, J.-C. G.; Pattison, P., *Chem. Sci.* **2012,** *3*, 384-390.

(3) Kuang, X.; Green, M. A.; Niu, H.; Zajdel, P.; Dickinson, C.; Claridge, J. B.; Jantsky, L.; Rosseinsky, M. J., *Nat Mater* **2008,** *7*, 498-504.

(4) Packer, R. J.; Skinner, S. J.; Yaremchenko, A. A.; Tsipis, E. V.; Kharton, V. V.; Patrakeev, M. V.; Bakhteeva, Y. A., *J. Mater. Chem.* **2006,** *16*, 3503-3511.

(5) Muktha, B.; Madras, G.; Guru Row, T. N., *J. Photochem. Photobiol., A* **2007,** *187*, 177-185.

(6) Parchur, A. K.; Ningthoujam, R. S., *Dalton Trans.* **2011,** *40*, 7590-7594.

(7) Yan, S.; Zhang, J.; Zhang, X.; Lu, S.; Ren, X.; Nie, Z.; Wang, X., *J. Phys. Chem. C* **2007,** *111*, 13256-13260.

(8) Bosbach, D.; Rabung, T.; Brandt, F.; Fanghänel, T., *Radiochim. Acta* **2004,** *92*, 639-643.

(9) Mendoza, C.; de Ligny, D.; Panczer, G.; Peuget, S.; Bardez-Giboire, I.; Schuller, S., *Opt. Mater.* **2011,** *34*, 386-390.

(10) Taurines, T.; Boizot, B., *J. Am. Ceram. Soc.* **2012,** *95*, 1105-1111.

(11) Patel, K. B.; Boizot, B.; Facq, S. P.; Lampronti, G. I.; Peuget, S.; Schuller, S.; Farnan, I., *Inorg. Chem.* **2017,** *56*, 1558-1573.

(12) Brinkman, K.; Fox, K.; Marra, J.; Reppert, J.; Crum, J.; Tang, M., *J. Alloys Compd.* **2013,** *551*, 136-142.

(13) Bruno, J.; Bosbach, D.; Kulik, D. A.; Navrotsky, A., *Chemical Thermodynamics of Solid Solutions of Interest in Nuclear Waste Management*. OECD Publishing: London, 2007; Vol. 10.

(14) Hsu, L.; Galli, P., *Econ. Geol.* **1973,** *68*, 681-696.

(15) Wesolowski, D.; Ohmoto, H., *Econ. Geol.* **1986,** *81*, 471-477.

(16) Shannon; R, *Acta Crystallogr., Sect. A* **1976,** *32*, 751-767.

(17) Marques Fernandes, M.; Schmidt, M.; Stumpf, T.; Walther, C.; Bosbach, D.; Klenze, R.; Fanghänel, T., *J. Colloid Interface Sci.* **2008,** *321*, 323-331.

(18) Schmidt, M.; Stumpf, T.; Walther, C.; Geckeis, H.; Fanghanel, T., *Dalton Trans.* **2009**, 6645-6650.

(19) Tu, D.; Liu, Y.; Zhu, H.; Li, R.; Liu, L.; Chen, X., *Angew. Chem. Int. Ed.* **2013,** *52*, 1128-1133.

(20) Huittinen, N.; Arinicheva, Y.; Schmidt, M.; Neumeier, S.; Stumpf, T., *J. Colloid Interface Sci.* **2016,** *483*, 139-145.

(21) Jones, G. D.; Peled, S.; Rosenwaks, S.; Yatsiv, S., *Phys. Rev.* **1969,** *183*, 353-368.

(22) Merz, J. L.; Pershan, P. S., *Phys. Rev.* **1967,** *162*, 235-247.

(23) Hanuza, J.; Haznar, A.; Maczka, M.; Pietraszko, A.; Lemiec, A.; Van der Maas, J.; Lutz, E., *J. Raman Spectrosc.* **1997,** *28*, 953-963.

(24) Kolitsch, U., *Z. Kristallogr. Cryst. Mater.* **2001,** *216*, 449-454.

(25) Macalik, L.; Hanuza, J.; Macalik, B.; Strek, W.; Legendziewicz, J., *Eur. J. Solid State Inorg. Chem.* **1996,** *33*, 397-410.

(26) Schmidt, M.; Stumpf, T.; Marques Fernandes, M.; Walther, C.; Fanghänel, T., *Angew. Chem. Int. Ed.* **2008,** *47*, 5846-5850.

(27) Andrade, L. H. d. C.; Li, M. S.; Guyot, Y.; Brenier, A.; Boulon, G., *J. Phys.: Condens. Matter* **2006,** *18*, 7883.

(28) Morozov, V. A.; Mironov, A. V.; Lazoryak, B. I.; Khaikina, E. G.; Basovich, O. M.; Rossell, M. D.; Van Tendeloo, G., *J. Solid State Chem.* **2006,** *179*, 1183-1191.

(29) Longo, V. M.; Figueiredo, A. T. d.; Campos, A. B.; Espinosa, J. W. M.; Hernandes, A. C.; Taft, C. A.; Sambrano, J. R.; Varela, J. A.; Longo, E., *J. Phys. Chem. A* **2008,** *112*, 8920-8928.

(30) Marques, A. P. A.; Picon, F. C.; Melo, D. M. A.; Pizani, P. S.; Leite, E. R.; Varela, J. A.; Longo, E., *J. Fluoresc* **2008,** *18*, 51-59.

(31) Vinograd, V. L.; Bosbach, D.; Winkler, B.; Gale, J. D., *Phys. Chem. Chem. Phys.* **2008,** *10*, 3509-3518.

(32) Schmidt, M.; Heck, S.; Bosbach, D.; Ganschow, S.; Walther, C.; Stumpf, T., *Dalton Trans.* **2013,** *42*, 8387-8393.

(33) Abakumov, A. M.; Morozov, V. A.; Tsirlin, A. A.; Verbeeck, J.; Hadermann, J., *Inorg. Chem.* **2014,** *53*, 9407-9415.

(34) Arakcheeva, A.; Logvinovich, D.; Chapuis, G.; Morozov, V.; Eliseeva, S. V.; Bunzli, J.-C. G.; Pattison, P., *Chemical Science* **2012,** *3*, 384-390.

(35) Brecher, C., *J. Chem. Phys.* **1974,** *61*, 2297-2315.

(36) Arora, S. K.; Batra, N. M.; Rao, G. S. T., *J. Am. Ceram. Soc.* **1985,** *68*, C-240--C-241-C.

(37) Cavalli, E.; Boutinaud, P.; Mahiou, R.; Bettinelli, M.; Dorenbos, P., *Inorg. Chem.* **2010,** *49*, 4916-4921.

(38) Sheldrick, G. M., *Acta Crystallogr., Sect. A* **2008,** *64*, 112-122.

(39) Aleksandrov, V.; Gorbatyii, L.; Ilyukhin, V., *Soviet Physics-Crystallography* **1968,** *13*, 414-415.

(40) Barkleit, A.; Foerstendorf, H.; Li, B.; Rossberg, A.; Moll, H.; Bernhard, G., *Dalton Trans.* **2011,** *40*, 9868-9876.

(41) Guckel, K.; Tsushima, S.; Foerstendorf, H., *Dalton Trans.* **2013,** *42*, 10172-10178.

(42) Schmeide, K.; Gürtler, S.; Müller, K.; Steudtner, R.; Joseph, C.; Bok, F.; Brendler, V., *Appl. Geochem.* **2014,** *49*, 116-125.

(43) Hellebrandt, S. E.; Hofmann, S.; Jordan, N.; Barkleit, A.; Schmidt, M., *Sci. Rep.* **2016,** *6*, 33137.

(44) Binnemans, K., *Coord. Chem. Rev.* **2015,** *295*, 1-45.

(45) Binnemans, K.; Görller-Walrand, C., *J. Rare Earth.* **1996,** *14*, 173-180.

(46) Lavín, V.; Rodríguez-Mendoza, U. R.; Martín, I. R.; Rodríguez, V. D., *J. Non-Cryst. Solids* **2003,** *319*, 200-216.

(47) Reisfeld, R.; Velapoldi, R. A.; Boehm, L.; Ish-Shalom, M., *J. Phys. Chem.* **1971,** *75*, 3980-3983.

(48) Cano-Torres, J. M.; Serrano, M. D.; Zaldo, C.; Rico, M.; Mateos, X.; Liu, J.; Griebner, U.; Petrov, V.; Valle, F. J.; Galán, M., *JOSA B* **2006,** *23*, 2494-2502.

(49) Rico, M.; Griebner, U.; Petrov, V.; Ortega, P.; Han, X.; Cascales, C.; Zaldo, C., *JOSA B* **2006,** *23*, 1083-1090.

(50) Schmidt, M.; Stumpf, T.; Walther, C.; Geckeis, H.; Fanghänel, T., *J. Colloid Int. Sci.* **2010,** *351*, 50-56.

(51) Görller-Walrand, C.; Binnemans, K., Rationalization of Crystal-Field Parametrization. In *Handbook on the Physics and Chemistry of Rare Earths*, K.A. Gschneidner, J.; Eyring, L., Eds. Elsevier Science B.V.: Amsterdam, 1996; Vol. 23, pp 121-284.

(52) Van Uitert, L., *J. Electrochem. Soc.* **1963,** *110*, 46-51.

For Table of Contents Only

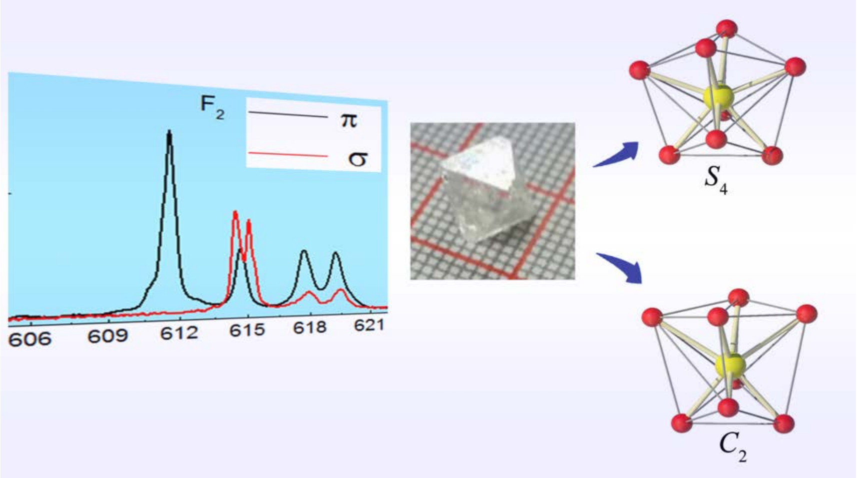

Synopsis

The local environment of a series of Eu^{3+} doped scheelite-type ABO_4 (A = Ca^{2+}, Sr^{2+}, Ba^{2+}; B = W^{6+}, Mo^{6+}) single crystals are systematically investigated using polarization-dependent TRLFS. The polarized fluorescence emission spectra demonstrate a strong dependence of the dopant site symmetry on the cation and anion in the different host matrices.